Incongruent Melting and Vitrification Behaviors of Anionic Coordination Polymers Incorporating Ionic Liquid Cations

Mochida, Tomoyuki
Qiu, Yi
Sumitani, Ryo
Kimata, Hironori
Furushima, Yoshitomo

(Citation)
Inorganic Chemistry,61(36):14368-14376

(Issue Date)
2022-09-12

(Resource Type)
journal article

(Version)
Accepted Manuscript

Incongruent Melting and Vitrification Behaviors of Anionic Coordination Polymers Incorporating Ionic Liquid Cations

Tomoyuki Mochida,*[†‡] Yi Qiu,[†] Ryo Sumitani,[†] Hironori Kimata,[†] and Yoshitomo Furushima[#]

[†]*Department of Chemistry, Graduate School of Science, Kobe University, 1-1 Rokkodai, Nada, Kobe, Hyogo 657-8501, Japan. E-mail: tmochida@platinum.kobe-u.ac.jp*

[‡]*Research Center for Membrane and Film Technology, Kobe University, 1-1 Rokkodai, Nada, Kobe, Hyogo 657-8501, Japan*

[#]*Materials Characterization Laboratories, Toray Research Center Inc., 3-7, Sonoyama 3-chome, Otsu, Shiga 520-8567, Japan*

Abstract: Several meltable coordination polymers (CPs) that possess substantial advantages attributable to their high flexibility and processability have been developed recently; however, the melting mechanism and vitrification conditions of these materials are not yet fully understood. In this study, we synthesized meltable CPs [A][K(TCM)$_2$] (A = onium cation, TCM = C(CN)$_3^-$) incorporating ionic liquid components and investigated their crystal structures and melting behaviors in detail. These CPs

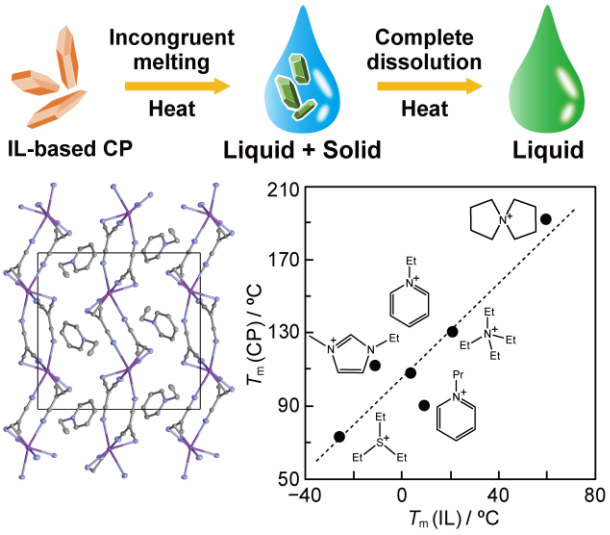

feature two- or three-dimensional anionic $[K(TCM)_2]^-_n$ frameworks incorporating onium cations. Each CP was found to undergo incongruent melting at a temperature between 73 and 192 °C to produce a heterogeneous mixture of the ionic liquid ([A][TCM]) and microcrystalline K[TCM]. Furthermore, they formed homogeneous liquids upon further heating to ~240 °C. The melting points of these CPs were linearly correlated with those of their constituent ionic liquids. The vitrification of these materials upon rapid cooling from the molten state was further investigated. The cooling rates required for vitrification differed greatly between the CPs and were correlated with the cation flexibility.

INTRODUCTION

In recent decades, coordination polymers (CPs), including metal–organic frameworks (MOFs), have attracted growing attention because of their useful functions, such as gas absorption and catalytic properties.[1] Although typical CPs do not melt and only undergo thermal decomposition at high temperatures, several meltable CPs have been reported to exhibit useful glass-forming properties, phase transformations, and processability.[2–4] In addition, CP glasses exhibit various structural and ion-transport properties that can be modified through doping, hybridization, and defect control. The majority of meltable CPs known to date possess one-dimensional (1D) structures, and many are structurally related to ionic liquids (ILs),[5] as exemplified by [1-butyl-4-methylpyridinium][$Cu(SCN)_2$][5a] and $[Emim]_2[MnN(CN)_4]$[5b] (Emim = 1-ethyl-3-methylimidazolium). In contrast, fewer two- and three-dimensional (2D and 3D) CPs have been reported, and these materials typically display higher melting points.[6,7,8] Representative examples are $[Zn(H_2PO_4)_2(triazole)_2]$ (T_m = 184 °C)[6a] and [$Zn(imidazolate)_2$] (ZIF-4; T_m = 593 °C).[7a] Although studies are ongoing into the development and application of

meltable CPs, the underling mechanism of the melting phenomenon has yet to be fully understood.

As part of our ongoing investigation into organometallic ILs,[9] we previously synthesized a series of meltable CPs, namely [A][MX_2] (A = organometallic cation; M = alkali metal ion, X = polycyano anion) from organometallic ILs (AX) and metal salts (MX).[10] These IL-containing CPs feature an anionic $[MX_2]^-_n$ framework with embedded organometallic cations (A). Their melting points ranged between 102–239 °C, and some of them underwent incongruent melting to give a solid–liquid mixture of the corresponding disproportionation products upon melting. It should be noted that the incongruent melting phenomenon has been observed for certain minerals, alloys, and metal salts but is extremely rare for CPs.[11] To investigate the mechanistic details of the melting behavior, we recently synthesized a CP containing an onium cation, [Emim][$K(TCM)_2$] (**1-Emim**; TCM = $C(CN)_3^-$).[12] This IL-containing CP was found to exhibit incongruent melting at 112 °C, while further heating to 240 °C afforded a homogeneous liquid phase, which underwent vitrification upon rapid cooling (T_g = −28 °C). Since incongruent melting was considered a relatively common phenomenon for meltable CPs, we aimed to synthesize a series of CPs with different cations to systematically understand their melting and vitrification mechanism.

Thus, we herein discuss the crystal structures and thermal behaviors of IL-containing CPs with the formula [cation][$K(TCM)_2$] (cation = $Emim^+$, $EtPy^+$, $PrPy^+$, $N(C_4H_8)_2^+$, NEt_4^+, or SEt_3^+; abbreviated as **1-cation**; **Figure 1**); note that the synthesis and properties of **1-Emim** have been communicated previously.[12] These anionic CPs were prepared from onium ILs ([cation][TCM][13]) and K[TCM] (**Figure 1**), and their thermal properties are investigated using differential scanning calorimetry (DSC) and fast scanning calorimetry (FSC). FSC is a powerful tool for investigating

fast thermodynamical phenomena.[14] Unlike previous research describing that incorporates ILs into the pores of MOFs to facilitate their melting,[15] our material design relies on the incorporation of the IL components into the CP framework to achieve meltability.[10] One related study is that has been reported recently is the preparation of CPs from fluorine-containing ILs and metal salts.[16] As structurally related compounds, many anionic CPs containing onium cations have been reported, which are regarded as dense MOFs.[17,18] Among them, the melting and vitrification of [cation][M(dicyanamide)$_3$] has been reported.[19] In addition, the preparation of lanthanide-TCM CPs using ILs has been reported recently.[20]

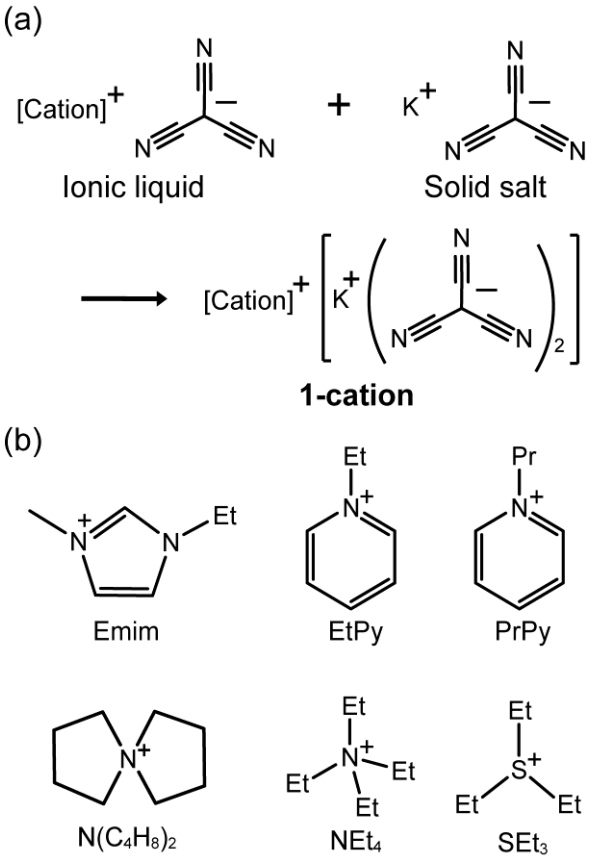

Figure 1. (a) Schematic outline of our route to preparation of the IL-containing CPs (**1-cation**) from [cation][TCM] and K[TCM]. (b) Various cations used for preparation of the CPs.

RESULTS AND DISCUSSION

Preparation. The recrystallization of [cation][TCM] and K[TCM] from Et_2O/EtOH afforded the desired CPs as colorless crystals in yields of 26–68%. The obtained crystals were stable under air, although **1-SEt$_3$** was somewhat hygroscopic. The mechanochemical preparation of the target CPs was also examined, wherein **1-Emim** was formed quantitatively by grinding a 1:1 mixture of liquid [Emim][TCM] and solid K[TCM] for 15 min using a mortar and pestle.[12] Although $[N(C_4N_8)_2][C(CN)_3]$ was solid at room temperature (T_m = 59.5 °C; crystal structure shown in **Figure S1**, supporting information), this salt also underwent the solvent-free reaction; 30 min grinding with K[TCM] under ambient conditions qualitatively produced **1-N(C$_4$H$_8$)$_2$**, as confirmed by powder X-ray diffraction (PXRD) measurements (**Figure S2**, supporting information). However, this solid-solid reaction did not proceed under an argon atmosphere, which suggests that the reaction is humidity-assisted, similar to the case of solvent-assisted solid-state reactions.[21]

Crystal structures. Crystal structure analysis of the CPs was performed at −173 °C, revealing anionic $[K(TCM)_2]^-_n$ framework structures incorporating onium cations. Except for the 3D structure obtained for **1-NEt$_4$**, all framework structures were 2D in nature. The assembled structures, structural parameters, and cation volumes of the CPs are summarized in **Table 1**. They are non-porous as seen from their high packing indices (73.9–77.6%). Each structure featured one crystallographically independent cation and one crystallographically independent $K[TCM]_2$ unit.

Figure 2a shows the packing diagrams of the 2D CPs projected perpendicular to the stacking directions, wherein the onium cations were located between the 2D frameworks to form layered structures. **1-N(C$_4$H$_8$)$_2$** and **1-Emim**[12] crystallized in the *P*-1 space group, while **1-EtPy**

and **1-PrPy** were isomorphous and crystallized in the $P2_1/n$ space group, and **1-SEt$_3$** crystallized in the *Pnma* space group. The 2D coordination frameworks in these CPs possessed the same structures with a kdg net topology,[22] as exemplified by the structure of **1-SEt$_3$** (**Figure 2b**). The potassium ions in these frameworks exhibited six-coordinate, octahedral coordination geometries, and the K–N coordination distances were comparable to those in K[TCM] (i.e., 2.90 Å).[23] The framework geometry was somewhat flexible, as observed from the variation in the dihedral angles between the two crystallographically independent TCM anions in the sheet (6.5–40.1°, **Table 1**). The interlayer distance also varied between the CPs (**Table 1**), although no correlation was observed with the cation volume, likely due to the flexibility of the framework structure. Furthermore, the cation in **1-SEt$_3$** exhibited a two-fold disorder of the sulfur atom (occupancy ratio 0.83:0.17) and of each ethyl substituent (0.5:0.5), whereas no cation disorder was observed for the other CPs.

1-NEt$_4$ exhibited a 3D anionic framework with a flu-3,6-Pnma net topology and a $Pna2_1$ space group, as shown in **Figure 3**. This 3D framework structure is ascribed to the largest cation volume of this CP, considering the similar trend of dimensionality observed for the relevant CPs containing organometallic cations.[10] As in the case of the 2D CPs, the potassium ions in the framework of **1-NEt$_4$** possessed a six-coordinate, octahedral coordination geometry. The cations were located in 1D channels extending along the *a*-axis direction.

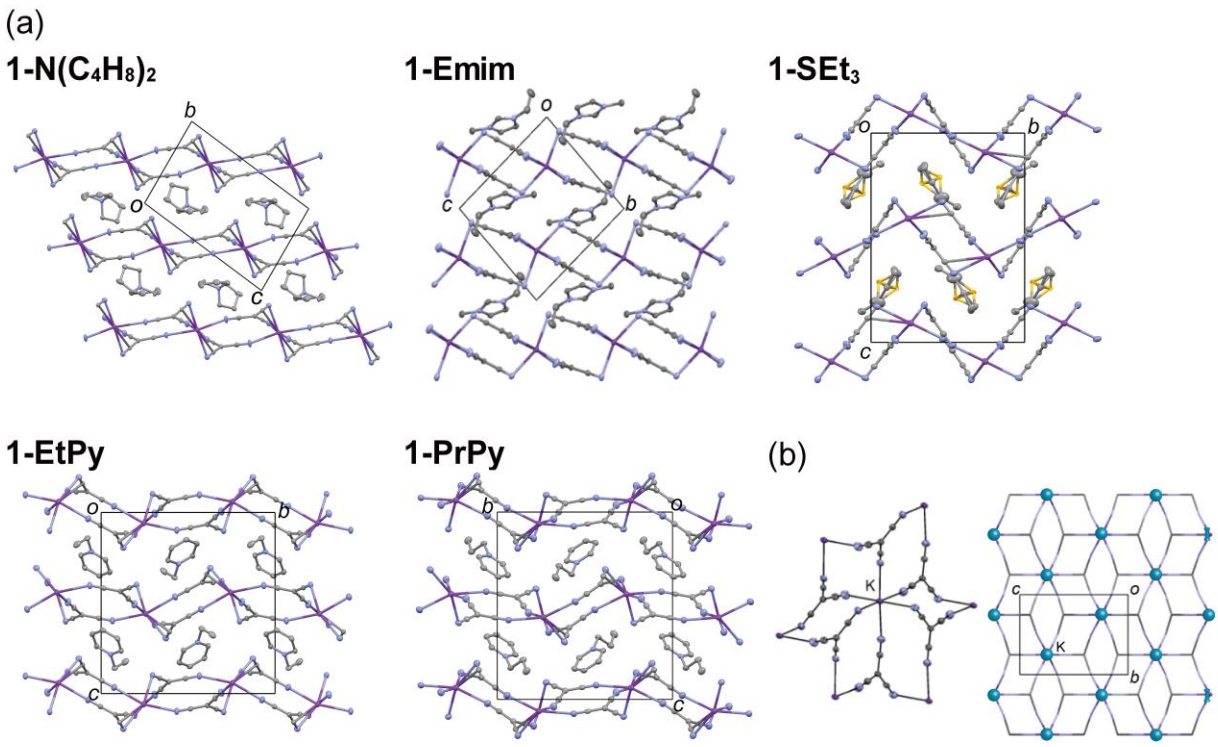

Figure 2. (a) Packing diagrams of the 2D CPs, namely **1-N(C$_4$H$_8$)$_2$**, **1-Emim**,[12] **1-EtPy**, **1-PrPy**, and **1-SEt$_3$**, projected parallel to the 2D framework, with layers stacked along the vertical direction. (b) The coordination sheet in **1-SEt$_3$** (left) and a diagram showing its kdg topology (right).

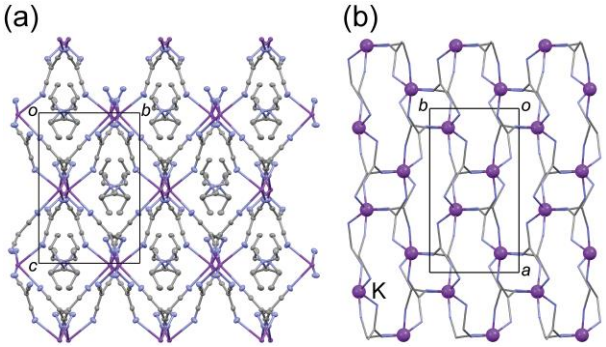

Figure 3. (a) Packing diagram of the 3D CP **1-NEt$_4$**, and (b) the topology of the coordination framework (flu-3,6-Pnma) therein.

Table 1. Assembled structures, structural parameters, and cation volumes of the prepared CPs

	space group	framework structure	framework topology	interlayer distance [Å]	dihedral angle[b] [°]	packing index [%]	cation volume[c] [Å^3]
1-N(C$_4$H$_8$)$_2$	*P*-1	2D	kdg	7.41	6.5	77.6	154.7
1-Emim[a]	*P*-1	2D	kdg	7.86	10.6	75.9	135.2
1-EtPy	$P2_1/n$	2D	kdg	7.24	35.9	73.9	133.3
1-PrPy	$P2_1/n$	2D	kdg	7.32	40.1	76.0	151.7
1-SEt$_3$	*Pnma*	2D	kdg	8.24	45.6	–[d]	148.9
1-NEt$_4$	$Pnm2_1$	3D	flu-3,6-Pnma	–	60.8	74.6	175.8

[a]Ref. 12. [b]Dihedral angle between two crystallographically independent TCM anions in the framework. [c]Volume of the onium cation estimated by DFT calculations (*ω*B97-D/LanL2DZ). [d]Not calculated because of the disordered structure.

POM observations of the melting behaviors. The melting behaviors of the CPs were observed under polarized optical microscopy (POM). The CPs underwent incongruent melting (T_m = 73–192 °C, determined by DSC) to produce a liquid–solid mixture upon melting, while further heating to 240 °C produced a uniform liquid, except for the less thermally stable **1-SEt$_3$**. In addition, the thermal stabilities of **1-SEt$_3$** and **1-Emim** were investigated by thermogravimetric (TG) analysis.

The POM images of **1-N(C$_4$H$_8$)$_2$** and **1-PrPy** taken at different temperatures are shown in **Figure 4**. Upon heating, **1-N(C$_4$H$_8$)$_2$** and **1-PrPy** exhibited incongruent melting at 192 and 90 °C, respectively, where melting was followed by the immediate deposition of K[TCM] microcrystals (**Figures 4a-ii** and **4b-ii**). The deposition of K[TCM], as confirmed by Raman and PXRD experiments for **1-Emim**,[12] is ascribed to its low solubility in the IL phase. Upon further heating, these microcrystals gradually dissolved into the liquid phase to give a homogeneous liquid phase at 230–240 °C (**Figures 4a-iii** and **4b-iii**). Upon cooling, the liquids solidified at ~165 and 73 °C, respectively, to form solid–liquid mixtures containing solid CP and K[TCM] (**Figures 4a-iv** and

4b-iv). Upon renewed heating, the CP present in the mixture underwent incongruent melting at the same temperatures detailed above (**Figures 4a-v** and **4b-v**). The observed melting and crystallization behaviors are schematically illustrated in **Figure 5**; these behaviors were confirmed by DSC and FSC as discussed below. It should be noted that **1-Emim**, **1-EtPy**, and **1-NEt$_4$** also exhibited comparable behaviors, undergoing incongruent melting at 112, 108, and 131 °C, respectively (**Figure S3**, supporting information).

1-SEt$_3$ underwent incongruent melting at 73 °C, which is the lowest melting temperature among the current CPs. However, upon further heating above 180 °C, this CP gradually turned red and decomposed before the formation of a homogeneous solution could take place (**Figure S4**, supporting information). Indeed, TG analysis revealed the thermal instability of this CP. The TG traces of **1-SEt$_3$**, **1-Emim**, and their constituent ILs are presented in **Figure 6**, in which **1-SEt$_3$** displayed a two-step weight loss, namely an initial small weight loss at ~120 °C and a second higher weight loss between 170 and 260 °C. The decomposition temperature (T_{dec}, −5% weight loss temperature) was 147 °C, and [SEt$_3$][TCM] exhibited a similar weight-loss behavior (T_{dec} = 170 °C). On the other hand, **1-Emim** was significantly more thermally robust (T_{dec} = 352 °C), exhibiting a TG trace similar to that of [Emim][TCM] (T_{dec} = 326 °C). These results therefore indicate that the thermal stability of the CP depends on the stability of the IL cation.

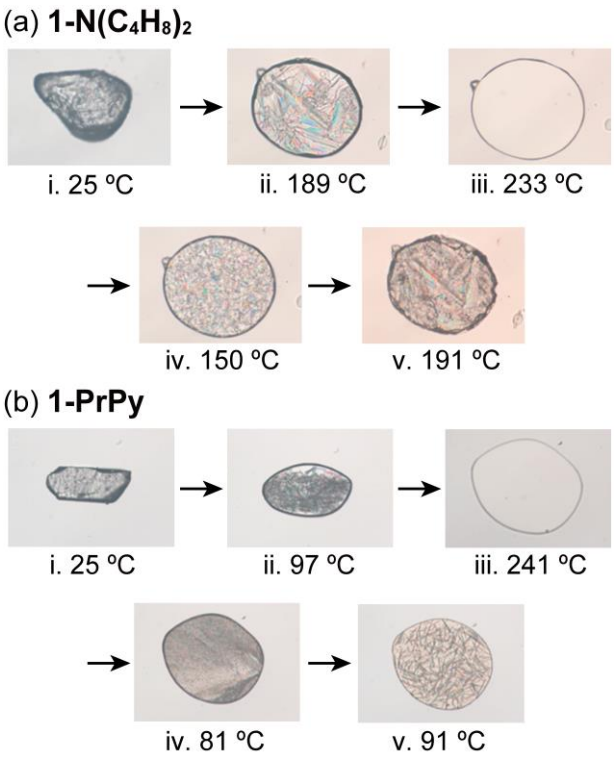

Figure 4. POM images of (a) **1-PrPy** and (b) **1-N(C4H8)2** at different temperatures: i) The crystalline state, ii) incongruent melting, iii) complete melting, iv) solidification (image acquired upon cooling of the liquid), and v) incongruent melting (image acquired upon solid reheating). The heating and cooling rates were both 20 K min^{-1}.

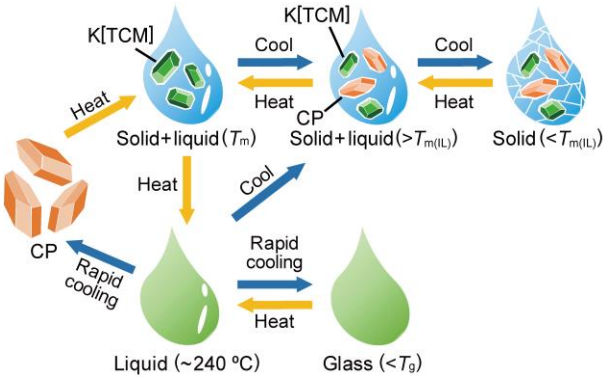

Figure 5. Schematic representation of the typical phase behavior of the CP system. Rapid cooling of the liquid gives a CP, glass, or their mixture depending on the compound and its

cooling rate. Non-equilibrium processes involving metastable states (such as cold crystallization) are not included to avoid complexity.

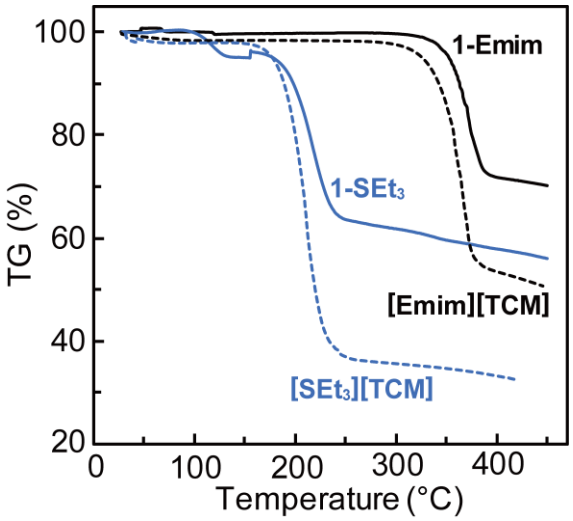

Figure 6. TG traces of **1-SEt$_3$** (solid blue line), [SEt$_3$][TCM] (dashed blue line), **1-Emim** (solid black line), and [Emim][TCM] (dashed black line) measured at 10 K min^{-1}. The step seen at 150 °C for **1-SEt$_3$** is an artifact.

DSC investigations of the melting behaviors. The thermodynamical behaviors of the CPs were investigated by DSC. The incongruent melting points of the CPs and their related parameters are listed in **Table 2**, while **Figure 7** presents the DSC traces of **1-N(C$_4$H$_8$)$_2$** and **1-PrPy**. The other CPs exhibited similar behaviors (**Figure S5**, supporting information).

Upon heating, **1-N(C$_4$H$_8$)$_2$** and **1-PrPy** displayed incongruent melting peaks in the DSC traces at 192 and 80 °C, respectively (**Figure 7**). Upon cooling the resultant solid–liquid mixture, partial crystallization of these CPs was observed at ~165 and 73 °C, respectively. In the second cycle, the CP components exhibited incongruent melting once again upon heating, albeit with smaller peak areas. The ratios of the second-cycle melting enthalpy ($\Delta H_m'$) to the first-cycle

melting enthalpy (ΔH_m) were 0.59 and 0.40, respectively (**Table 2**), which indicates that roughly half of the CP was re-formed upon cooling, whereas the rest remained in the form of the disproportionation products (K[TCM] and [cation][TCM]). Indeed, the crystallization and melting of the remaining IL components were observed in the DSC traces, as indicated by the solid triangles shown in **Figure 7**. The same tendency was observed for the other CPs, wherein the values of $\Delta H_m'/\Delta H_m$ ranged from 0.40 to 0.57, and the melting points of the IL components ($T_{m(IL/CP)}$) generated upon incongruent melting were between −7.0 and 56.3 °C; in each case, this temperature was close to that of pure IL ($T_{m(IL)}$, **Table 2**). With further heating above the incongruent melting point, a broad endothermic peak was observed in the DSC chart up to ~240 °C, which is attributed to the dissolution of K[TCM]. Cooling the melt at a rate of 10 K min^{-1} to ambient temperature also produced the corresponding liquid−solid mixture containing solid CP and K[TCM].

In addition to the peaks related to incongruent melting, solid-phase transitions were observed for **1-Emim** and **1-NEt$_4$** at 68.9 °C (ΔH = 5.1 kJ K^{-1} mol^{-1})[12] and 111.3 °C (ΔH = 9.4 kJ K^{-1} mol^{-1}), respectively, which are considered to originate from cation disorder. The incongruent melting enthalpy (ΔH_m), which represented the sum of the melting and K[TCM] deposition enthalpies, fell within the range of 9.4–37.2 kJ mol^{-1} for the CPs examined herein (**Table 2**). Notably, **1-NEt$_4$** (ΔH_m = 9.4 kJ mol^{-1}) and **1-SEt$_3$** (ΔH_m = 18.3 kJ mol^{-1}) exhibited rather small ΔH_m values, which were ascribed to their solid-phase transition and cation disorder, respectively.

Table 2. Thermodynamic data for the CPs and their constituent ILs obtained by DSC and FSC

	DSC data						FSC data	
	T_m [°C]	ΔH_m [kJ mol^{-1}]	$\Delta H_m'/\Delta H_m$[a]	T_{cryst}[b] [°C]	$T_{m(IL/CP)}$[c] [°C]	$T_{m(IL)}$[d] [°C]	T_{cryst}[e] [°C]	Cooling rate[f] [°C s^{-1}]
1-N(C$_4$H$_8$)$_2$	191.6	37.2	0.59	165	56.3	59.5		(> 5000)[k]
1-Emim[g]	112.3	20.6	0.44	99	−6.8	−11[h]	50	30–200
1-EtPy	107.7	26.8	0.54	100	4.0	3.7	40	300–1000
1-PrPy	89.9	28.9	0.40	73	6.3	(9)[i]	60	10–30
1-NEt$_4$	130.6	9.4	0.57	116	30.2	21.1		
1-SEt$_3$	73.3	18.3	0.45	50	−7.0	(−25.9)[j]		

[a]Ratio of the incongruent melting entropy in the second cycle to that in the first cycle. [b]Crystallization temperature (peak maximum) of the CP component observed upon cooling immediately after incongruent melting. [c]Observed melting point of the IL component in the CP. [d]Melting point of the pure IL ([cation][TCM]). [e]Cold-crystallization temperature (peak maximum) observed upon heating from the completely vitrified state. [f]Range of the cooling rate in which partial to complete vitrification occurs. [g]Ref. 12. [h]Ref. 24. [i]Predicted from the glass transition temperature (T_g = −85 °C) based on the empirical relationship of T_g/T_m = 2/3. [j]Predicted value (ref. 25). [k]No vitrification observed at cooling rates up to 5000 K s^{-1}.

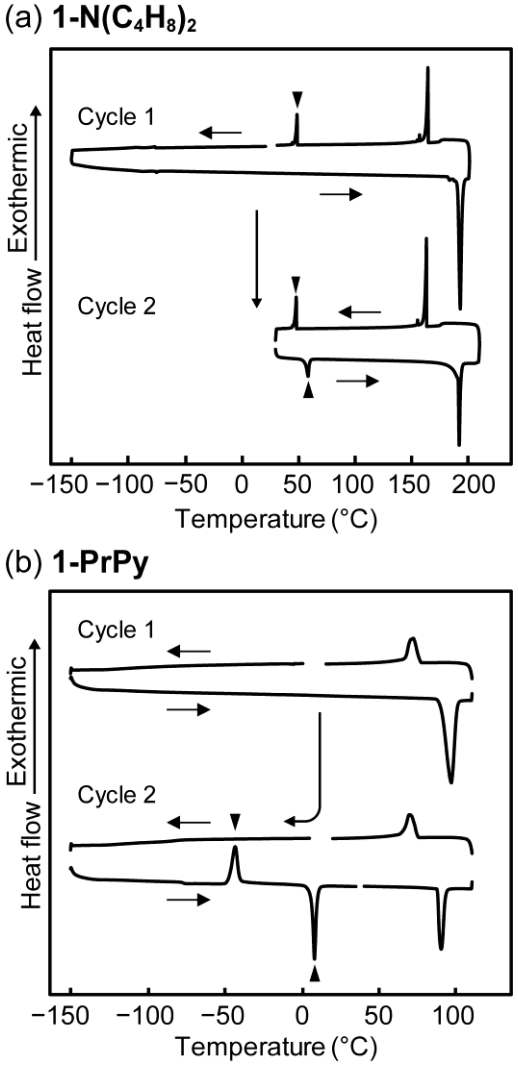

Figure 7. DSC traces of (a) **1-N(C$_4$H$_8$)$_2$** and (b) **1-PrPy**. The solid triangles indicate solidification and melting of the IL component.

Comparison of the melting and crystallization temperatures. The factors determining the melting points and crystallization behaviors of the CPs were then investigated. DSC measurements revealed that the melting points (T_m) of the CPs varied significantly (73–192 °C), although the majority of them exhibited the same 2D framework structures. In **Figure 8,** the linear relationship between the melting points of the CPs (T_m) versus those of the

constituent ILs can be seen ($T_{m(IL)}$, **Table 2**). There was no correlation between T_m and the cation volume, framework dimensions, or packing index (**Table 1**).

Furthermore, we found that the ease of CP crystallization was correlated with the cation structure. As shown in the DSC measurements, crystallization was observed for all CPs during cooling after incongruent melting. The crystallization temperatures (T_{cryst}) increased in the order **1-SEt$_3$** (50 °C) < **1-PrPy** (73 °C) < **1-Emim** (99 °C) ≈ **1-EtPy** (100 °C) < **1-NEt$_4$** (116 °C) < **1-N(C$_4$H$_8$)$_2$** (165 °C), indicating that crystallization becomes easier in this order. This trend is consistent with the cation flexibility. More specifically, among the N-containing 2D CPs, **1-N(C$_4$H$_8$)$_2$**, which contains a rigid cation, is the easiest to crystallize, followed by **1-EtPy** and **1-Emim**, which contain ethyl-substituted cations, and then **1-PrPy** with a propyl-substituted cation. This tendency is also in agreement with the crystallization tendency of the constituent ILs observed by DSC (**Figure S6**, supporting information); upon cooling from a melt at 10 K min^{-1}, [N(C$_4$H$_8$)$_2$][TCM] exhibited only crystallization, [EtPy][TCM] and [Emim][TCM][24] showed vitrification and cold crystallization, whereas [PrPy][TCM] underwent only vitrification. These results indicate that the melting points and crystallization tendencies of IL-containing CPs can be controlled by molecular design.

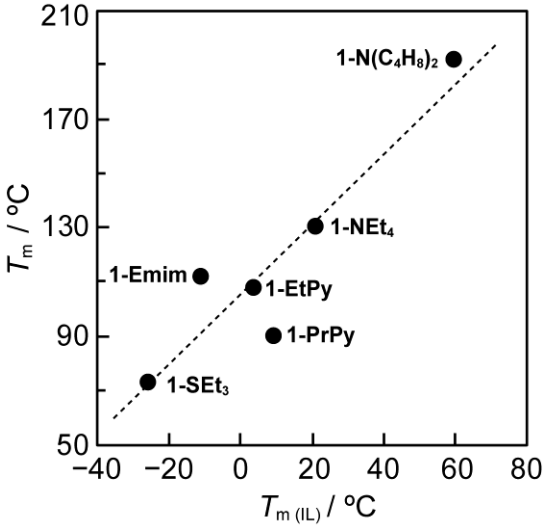

Figure 8. Correlation of the melting points of the CPs and their constituent ILs. The dotted line represents the least-squares fit.

FSC investigation of the vitrification behavior. Vitrification of the 2D CPs upon rapid cooling from the melt was investigated using FSC. It was found that **1-EtPy**, **1-Emim**, and **1-PrPy** vitrified upon rapid cooling, whereas **1-N(C_4H_8)$_2$** underwent only crystallization, even at the fastest cooling rate. The cooling rates required for vitrification differed greatly between the various CPs and appeared to depend on their cation structures.

The FSC data for **1-N(C_4H_8)$_2$**, **1-EtPy**, and **1-PrPy** are shown in **Figure 9**, whereas the data for **1-Emim** was reported previously.[12] The molten CPs were cooled from 250 to −85 °C at varying rates (5000–1 K s^{-1}), and the FSC data were collected during heating to 250 °C at 1000 K s^{-1}. In the DSC measurements, cooling of the CPs from the molten state at a rate of 10 K min^{-1} gave a mixture of the CP, K[TCM], and [cation][TCM] because of the high crystallinity of K[TCM]. However, we found that the significantly faster cooling employed for the FSC measurements resulted in complete crystallization of the CP, while a further increase in the cooling rate led to vitrification in most cases, as summarized schematically in **Figure 5**.

More specifically, **1-N(C_4H_8)$_2$** exhibited only incongruent melting peaks in the FSC traces, which indicates that the CP underwent only crystallization even when cooling at a rate of 5000 K s^{-1} (**Figure 9a**). In the case of **1-EtPy**, complete vitrification occurred at cooling rates of 3000 and 1000 K s^{-1}. Therefore, glass transition to a liquid, cold crystallization of the liquid, and incongruent melting of the crystal occurred successively upon heating, as observed in the FSC trace at ~26, 40, and 122 °C, respectively (**Figure 9b**). In addition, a broad endothermic peak attributed to the dissolution of K[TCM] into the liquid phase was observed at ~210 °C. However,

at cooling rates of 500 and 300 Ks^{-1}, partial crystallization occurred during cooling, resulting in a smaller cold crystallization peaks upon heating. Moreover, at slower cooling rates (100–1 K s^{-1}), complete crystallization occurred during cooling; consequently, only melting of the CP was observed in the FSC traces. **1-Emim** exhibited a similar behavior, with partial-to-complete vitrification occurring at cooling rates of 30–200 K s^{-1}.[12]

1-PrPy also formed a glass upon rapid cooling, and hence, a glass transition was observed in the FSC trace (**Figure 9c**). However, since this material is the least crystallizable of the CPs examined herein (as discussed above), no crystallization was observed during heating following cooling at rates of 5000–50 K s^{-1}. In this case, the sample cooled at 1000–50 K s^{-1} exhibited a broad exothermic peak due to the cold crystallization of K(TCM) at ~180 °C, while a broad endothermic peak due to the dissolution of K(TCM) was also observed at ~220 °C. When the sample was cooled at 30 and 10 K s^{-1}, nearly complete and partial vitrification occurred, and a peak corresponding to cold crystallization into the CP was also observed. The crystallization may be ascribed to the presence of crystal nuclei. Crystallization was complete following cooling at a rate of 5 K s^{-1}, and as a result, only a melting peak appeared in the FSC trace.

Despite the different melting points of **1-PrPy**, **1-Emim**, and **1-EtPy** (i.e., 89.9, 112.3, and 107.7 °C, respectively), their glass transition temperatures were comparable at −26, −26, and −28 °C, respectively. Their corresponding T_g/T_m values were calculated to be 0.68, 0.65, and 0.64, respectively, and these values are consistent with the empirical relationship $T_g/T_m = 2/3$.[26] However, the cooling rates required for vitrification differed greatly between these CPs, with the cooling rates required for partial-to-complete vitrification being approximately 10–30, 30–200, and 300–1000 K s^{-1}, respectively, indicating that glass formation becomes more difficult in this order. Furthermore, **1-N(C_4H_8)$_2$** did not undergo vitrification even upon cooling at a rate of 5000

K s^{-1}. Therefore, the cooling rates required for vitrification were consistent with the crystallization tendency, as discussed in the previous section. The cold crystallization temperatures observed in the FSC trace upon heating from the completely vitrified state decreased in the order **1-PrPy** (60 °C) > **1-Emim** (50 °C) > **1-EtPy** (40 °C), which is also consistent with this tendency. These results again indicate that the less flexible the cation is, the easier the crystallization. It should be noted that the ease of crystallization does not necessarily correlate with the melting point because crystallization is a kinetic phenomenon. Furthermore, there was also a correlation between the crystallization tendencies of these CPs and those of their constituent ILs, though the CPs required significantly faster cooling rates for vitrification than the ILs alone. These results suggest that the use of flexible, less rigid molecules is advantageous for promoting the vitrification of meltable CPs.

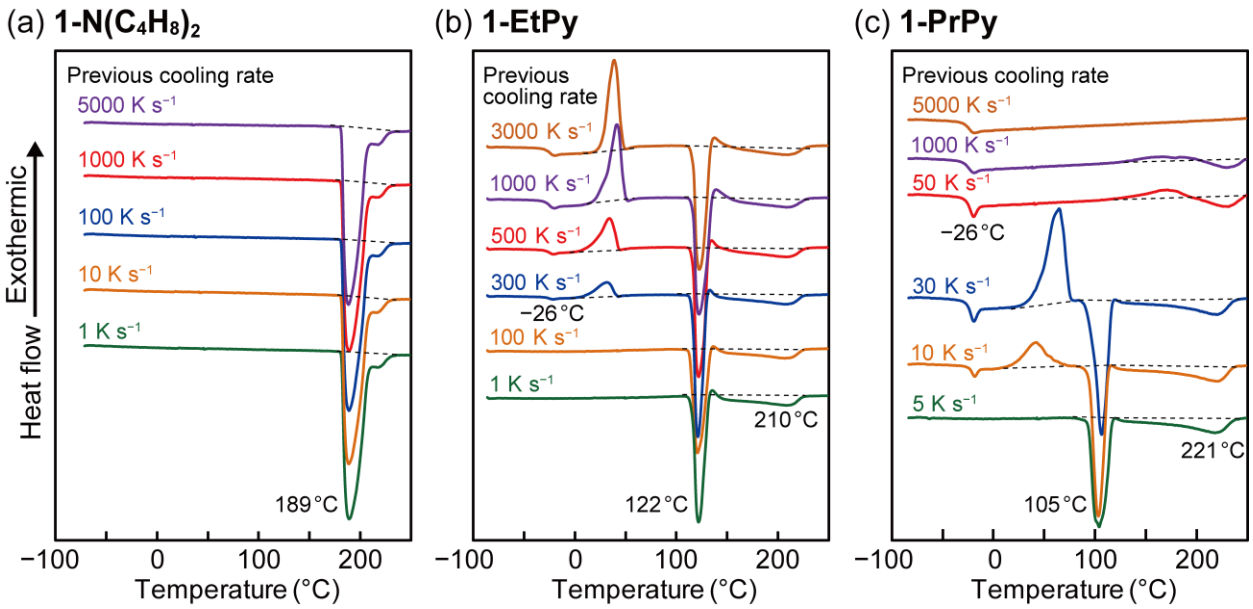

Figure 9. FSC traces of (a) **1-N(C_4H_8)$_2$**, (b) **1-EtPy**, and (c) **1-PrPy**. The data were recorded upon heating the samples at 1000 K s^{-1} after cooling from the molten state at various cooling rates (i.e., 1–5000 K s^{-1}). The cooling rates are indicated in the figure.

CONCLUSIONS

We synthesized a series of meltable CPs that exhibit incongruent melting. These CPs were prepared by the reaction of onium ILs with K[TCM], both containing TCM as a common ion. The mechanism of incongruent melting was investigated, and its generality in these IL-containing CPs was demonstrated. Furthermore, we elucidated the factors governing their melting and vitrification conditions. It was found that the melting points of the prepared CPs were linearly correlated with those of their constituent ILs, thereby indicating that low-melting-point CPs can be prepared from low-melting-point ILs. In addition, the cooling rate required for vitrification from the molten state, which differed greatly between CPs, was correlated with the cation flexibility due to its influence on the ease of crystallization. These results therefore indicate that the use of flexible, less rigid molecules is advantageous for designing meltable CPs with higher vitrification abilities. Incongruent melting remains rare in the context of CPs, but is a common phenomenon in multicomponent solids, such as alloys and minerals. Thus, we anticipate that incongruent melting will be more generally detected in meltable CPs in the future. Although the CPs prepared in this study were non-porous, future studies could focus on the development of IL-containing meltable porous MOFs. Finally, we expect that application of fast scanning calorimetry to coordination polymer research will be an important subject of future studies.

EXPERIMENTAL SECTION

General. [Emim][TCM] and [PrPy][TCM] were synthesized as described previously,[24,13] while the other ILs were prepared by dissolving equimolar amounts of their corresponding

onium halides and K[TCM] in water, followed by extraction with dichloromethane, concentration, and vacuum-drying, to give the desired products in yields of 30–80%. All chemicals were commercially available and were used as received. DSC measurements were performed using a TA Instruments Q100 differential scanning calorimeter at a sweep rate of 10 K min^{-1}. TG measurements were performed using a Rigaku TG8120 analyzer at a rate of 10 K min^{-1} under a nitrogen environment. The FT-IR spectra were recorded in the attenuated total reflectance mode (ATR diamond) on a Thermo Scientific Nicolet iS5 FT-IR spectrometer. PXRD measurements were performed using a Rigaku Smartlab diffractometer with Cu Kα radiation. The van der Waals volumes of the molecular ions were estimated by density functional theory (DFT) calculations (*ω*B97-D/LanL2DZ) using Spartan '20 software (Wavefunction, Inc.). The FSC measurements were conducted using a Mettler Toledo Flash DSC 1 instrument under a nitrogen atmosphere. For each sample, a single crystal was heated to 250 °C at a rate of 100 K min^{-1}, maintained at this temperature for 5 s, and then cooled to −85 °C at the desired cooling rate (1–5000 K s^{-1}). Subsequently, the FSC traces were recorded upon heating the sample to 250 °C at a rate of 1000 K s^{-1}. The measurements recorded at the various cooling rates were carried out using the same samples and were repeated for reproducibility.

Synthesis. **1-NEt_4** was obtained as colorless acicular crystals by slow cooling a solution of [NEt_4][TCM] (16.3 mg, 0.07 mmol) and K[TCM] (10 mg, 0.08 mmol) in Et_2O–EtOH to −40 °C. The crystals were collected by filtration and dried under vacuum (10.5 mg, 68%). Anal. Calcd. for $C_{16}H_{20}N_7K$: C, 54.99; H, 5.77; N, 28.06. Found: C, 55.09; H, 5.87; N, 28.02. IR (cm^{-1}): 2988, 2165(CN), 2129, 1482, 1453, 1438, 1393, 1367, 1234, 1172, 1055, 998, 967, 783, 562. The other complexes (colorless acicular crystals) were prepared by the same means from the corresponding [cation][TCM] ILs, with an Et_2O–MeOH solvent mixture being used in the preparation of

1-PrPy, **1-N(C_4H_8)$_2$**, and **1-SEt$_3$**. **1-EtPy** (58% yield): Anal. Calcd. for $C_{15}H_{10}N_7K$: C, 55.03; H, 3.08; N, 29.95. Found: C, 55.00; H, 2.74; N, 29.91. IR (cm^{-1}): 2163(CN), 1636, 1490, 1242, 1175, 777, 684, 564, 526. **1-PrPy** (29% yield): Anal. Calcd. for $C_{16}H_{12}N_7K$: C, 56.29; H, 3.54; N, 28.72. Found: C, 55.97; H, 3.04; N, 28.61. **1-N(C_4H_8)$_2$** (54% yield): Anal. Calcd. for $C_{16}H_{16}N_7K$: C, 55.63; H, 4.67; N, 28.38. Found: C, 55.64; H, 4.53; N, 28.19. IR (cm^{-1}): 3065, 2976, 2163(CN), 1636, 1583, 1506, 1490, 1456, 1389, 1314, 1237, 1221, 1171, 966, 823, 769, 686, 564. **1-SEt$_3$** (37% yield): Anal. Calcd. for $C_{14}H_{15}N_6SK$: C, 49.68; H, 4.47; N, 24.83. Found: C, 49.76; H, 4.17; N, 24.70. IR (cm^{-1}): 2942, 2161(CN), 1451, 1420, 1389, 1265, 1236, 1083, 977, 790, 564.

It should be noted here that we also attempted the above process using ILs containing other cations, such as Pmim (1-propyl-3-methyimidazolium cation), Bmim (1-butyl-3-methylimidazolium cation), DEME ($N^+MeEt_2CH_2CH_2OMe$), NPr_4^+, and NMe_4^+, but they failed to give the desired CPs. The use of $NMeEt_3^+$ produced a CP (T_m = 130.0 °C) that was isomorphous to **1-NEt$_4$**, but it is not discussed in the current study due to its poor crystal quality.

X-ray structure determination. The single-crystal X-ray diffraction data were collected on a Bruker APEX II Ultra CCD diffractometer at −173 °C using Mo K_α radiation (λ = 0.71073 Å). Single crystals of the CPs and [N(C_4H_8)$_2$][TCM] were obtained by recrystallization from Et_2O–MeOH or Et_2O–EtOH, as described above. All calculations were performed using SHELXTL.[27] Packing diagrams were drawn using Mercury software,[28] and the packing indices were calculated using Platon.[29] The crystallographic parameters are listed in **Tables S1** and **S2** (supporting information). CSD numbers: CCDC-1869225 (**1-EtPy**), 1893149 (**1-PrPy**), 1921331 (**1-N(C_4H_8)$_2$**), 1869224 (**1-NEt$_4$**), 1921330 (**1-SEt$_3$**), and 1992114 ([N(C_4H_8)$_2$][TCM]).

Conflict of interest

There are no conflicts to declare.

ASSOCIATED CONTENT

Supporting information

The Supporting Information is available free of charge at https://

Crystal structures; PXRD patterns; POM images; DSC charts; crystallographic parameters (PDF)

AUTHOR INFORMATION

Corresponding Author

Tomoyuki Mochida − *Department of Chemistry, Graduate School of Science and Research Center for Membrane and Film Technology, Kobe University, Kobe, Hyogo 657-8501, Japan;*

https://orcid.org/0000-0002-3446-2145; Phone: +81-78-803-5679;

Email: tmochida@platinum.kobe--u.ac.jp

Authors

Yi Qiu, Ryo Sumitani, Hironori Kimata − *Department of Chemistry, Graduate School of Science, Kobe University, Kobe, Hyogo 657-8501, Japan*

Yoshitomo Furushima − *Materials Characterization Laboratories, Toray Research Center Inc., 3-7, Sonoyama 3-chome, Otsu, Shiga 520-8567, Japan*

Notes

The authors declare no competing financial interest.

ACKNOWLEDGMENTS

This work was supported by the KAKENHI (Grant No. 20K21210) funded by the Japan Society for the Promotion of Science (JSPS).

REFERENCES

(1) (a) Kitagawa, S. Future Porous Materials. *Acc. Chem. Res.* **2017**, *50,* 514–516. (b) Furukawa, H.; Cordova, K. E.; O'Keeffe, M.; Yaghi, O. M. The Chemistry and Applications of Metal-Organic Frameworks. *Science* **2013**, *341,* 1230444. (c) Kole, G. K.; Vittal, J. J. Solid-State Reactivity and Structural Transformations Involving Coordination Polymers. *Chem. Soc. Rev.* **2013**, *42*, 1755–1775.

(2) Bennett, T. D.; Horike, S. Liquid, Glass and Amorphous Solid States of Coordination Polymers and Metal–Organic Frameworks. *Nat. Rev. Mater.* **2018**, *3*, 431–440.

(3) Ma, N.; Horike, S. Metal-Organic Network-Forming Glasses. *Chem. Rev.* **2022**, *122*, 4163–4203.

(4) Horike, S.; Nagarkar, S., S.; Ogawa, T.; Kitagawa, S. A New Dimension for Coordination Polymers and Metal-Organic Frameworks: Towards Functional Glasses and Liquids. *Angew. Chem., Int. Ed.* **2020**, 59, 6652–6664.

(5) (a) Spielberg, E. T.; Edengeiser, E.; Mallick, B.; Havenith, M.; Mudring, A.-V. (1-Butyl-4-Methyl-Pyridinium)[$Cu(SCN)_2$]: A Coordination Polymer and Ionic Liquid. *Chem. – Eur. J.* **2014**, *20,* 5338–5345. (b) Hiraoka, T.; Ohtani, R.; Nakamura, M.; Lindoy, L. F.; Hayami, S. Water-Induced Breaking of the Coulombic Ordering in a Room-Temperature Ionic Liquid Metal Complex. *Chem. – Eur. J.* **2019**, *25,* 7521–7525. (c) Moriya, M.; Kato, D.; Sakamoto, W.;

Yogo, T. Structural Design of Ionic Conduction Paths in Molecular Crystals for Selective and Enhanced Lithium Ion Conduction. *Chem. – Eur. J.* **2013**, *19*, 13554–13560.

(d) Hirai, Y.; Nakanishi, T.; Kitagawa, Y.; Fushimi, K.; Seki, T.; Ito, H.; Fueno, H.; Tanaka, K.; Satoh, T.; Hasegawa, Y. Luminescent Coordination Glass: Remarkable Morphological Strategy for Assembled Eu(III) Complexes. *Inorg. Chem.* **2015,** *54*, 4364–4370.

(e) Su, Y.-J.; Cui, Y.-L.; Wang, Y.; Lin, R.-B.; Zhang, W.-X.; Zhang, J.-P.; Chen, X.-M. Copper(I) 2-Isopropylimidazolate: Supramolecular Isomerism, Isomerization, and Luminescent Properties. *Cryst. Growth Des.* **2015**, *15*, 1735–1739. (f) Depuydt, D.; Brooks, N. R.; Schaltin, S.; Van Meervelt, L.; Fransaer, J.; Binnemans, K. Silver-Containing Ionic Liquids with Alkylamine Ligands. *ChemPlusChem* **2013**, *78*, 578–588.

(6) (a) Umeyama, D.; Horike, S.; Inukai, M.; Itakura, T.; Kitagawa, S. Reversible Solid-to-Liquid Phase Transition of Coordination Polymer Crystals. *J. Am. Chem. Soc.* **2015**, *137*, 864–870. (b) Umeyama, D.; Funnell, N. P.; Cliffe, M. J.; Hill, J. A.; Goodwin, A. L.; Hijikata, Y.; Itakura, T.; Okubo, T.; Horike, S.; Kitagawa, S. Glass Formation via Structural Fragmentation of a 2D Coordination Network. *Chem. Commun.* **2015**, *51*, 12728–12731. (c) Chen, W.; Horike, S.; Umeyama, D.; Ogiwara, N.; Itakura, T.; Tassel, C.; Goto, Y.; Kageyama, H.; Kitagawa, S. Glass Formation of a Coordination Polymer Crystal for Enhanced Proton Conductivity and Material Flexibility. *Angew. Chem. Int. Ed.* **2016**, *55*, 5195–5200. (d) Ohara, Y.; Hinokimoto, A.; Chen, W.; Kitao, T.; Nishiyama, Y.; Hong, Y.-L.; Kitagawa, S.; Horike, S. Formation of Coordination Polymer Glass by Mechanical Milling: Dependence on Metal Ions and Molecular Doping for H^+ Conductivity. *Chem. Commun.* **2018**, *54*, 6859–6862.

(7) (a) Bennett, T. D.; Tan, J.-C.; Yue, Y.; Baxter, E.; Ducati, C.; Terrill, N. J.; Yeung, H. H.-M.; Zhou, Z.; Chen, W.; Henke, S.; Cheetham, A. K.; Greaves, G. N. Hybrid Glasses from Strong and

Fragile Metal-Organic Framework Liquids. *Nat. Commun.* **2015**, *6*, 8079. (b) Gaillac, R.; Pullumbi, P.; Beyer, K. A.; Chapman, K. W.; Keen, D. A.; Bennett, T. D.; Coudert, F.-X. Liquid Metal-Organic Frameworks. *Nat. Mater.* **2017**, *16*, 1149–1154. (c) Bennett, T. D.; Yue, Y.; Li, P.; Qiao, A.; Tao, H.; Greaves, N. G.; Richards, T.; Lampronti, G. I.; Redfern, S. A. T.; Blanc, F.; Farha, O. K.; Hupp, J. T.; Cheetham, A. K.; Keen, D. A. Melt-Quenched Glasses of Metal-Organic Frameworks. *J. Am. Chem. Soc.* **2016**, *138*, 3484–3492. (d) Longley, L.; Collins, S. M.; Zhou, C.; Smales, G. J.; Norman, S. E.; Brownbill, N. J.; Ashling, C. W.; Chater, P. A.; Tovey, R.; Schönlieb, C.-B.; Headen, T. F.; Terrill, N. J.; Yue, Y.; Smith, A. J.; Blanc, F.; Keen, D. A.; Midgley, P. A.; Bennett, T. D. Liquid Phase Blending of Metal-Organic Frameworks. *Nat. Commun.* **2018**, *9*, 2135.

(8) (a) Tanaka, K.; Tago, Y.; Kondo, M.; Watanabe, Y.; Nishio, K.; Hitosugi, T.; Moriya, M. High Li-Ion Conductivity in $Li\{N(SO_2F)_2\}(NCCH_2CH_2CN)_2$ Molecular Crystal. *Nano Lett.* **2020**, *20*, 8200–8204. (b) Liu, M.; McGillicuddy, R. D.; Vuong, H.; Tao, S.; Slavney, A. H.; Gonzalez, M. I.; Billinge, S. J. L.; Mason, J. A. Network-Forming Liquids from Metal-Bis(Acetamide) Frameworks with Low Melting Temperatures. *J. Am. Chem. Soc.* **2021**, *143*, 2801–2811.

(9) (a) Inagaki, T.; Mochida, T.; Takahashi, M.; Kanadani, C.; Saito, T.; Kuwahara, D. Ionic Liquids of Cationic Sandwich Complexes. *Chem. Eur. J.* **2012**, *18*, 6795–6804. (b) Hamada, S.; Funasako, Y.; Mochida, T.; Kuwahara, D.; Yoza, K. Phase Transitions and Thermal Properties of Decamethylferrocenium Salts with Perfluoroalkyl-Sulfonate and -Carboxylate Anions Exhibiting Disorder. *J. Organomet. Chem.* **2012**, *713*, 35–41. (c) Funasako, Y.; Inagaki, T.; Mochida, T.; Sakurai, T.; Ohta, H.; Furukawa, K.; Nakamura, T. Organometallic Ionic Liquids from Alkyloctamethylferrocenium Cations: Thermal Properties, Crystal Structures, and Magnetic Properties. *Dalton Trans.* **2013**, *42*, 8317–8327. (d) Ueda, T.; Mochida, T. Thermal Properties

and Crystal Structures of Ionic Liquids from Ruthenium Sandwich Complexes with Trialkoxybenzene Ligands: Effects of Substituent Positions and Alkyl Chain Lengths. *Organometallics* **2015**, *34*, 1279–1286. (e) Higashi, T.; Ueda, T.; Mochida, T. Effects of Substituent Branching and Chirality on the Physical Properties of Ionic Liquids Based on Cationic Ruthenium Sandwich Complexes. *Phys. Chem. Chem. Phys.* **2016**, *18*, 10041–10048.

(10) Kimata, H.; Mochida, T. Crystal Structures and Melting Behaviors of 2D and 3D Anionic Coordination Polymers Containing Organometallic Ionic Liquid Components. *Chem. – Eur. J.* **2019**, *25*, 10111–10117.

(11) (a) Soldatov, D. V.; Ripmeester, J. A. Inclusion in Microporous β-Bis(1,1,1-Trifluoro-5,5-Dimethyl-5-Methoxyacetylacetonato)Copper(II), an Organic Zeolite Mimic. *Chem. Mater.* **2000**, *12*, 1827–1839. (b) Martínez Casado, F. J.; Ramos Riesco, M.; Da Silva, I.; Redondo Yélamos, M. I.; Labrador, A.; Cheda, J. A. R. Lithium and Lead(II) Butyrates Binary System. Pure Compounds and an Intermediate Salt: From 2D to 3D Coordination Polymers. *Cryst. Growth Des.* **2011**, *11*, 759–767. (c) Ukraintseva, E. A.; Soldatov, D. V.; Zelenina, L. N.; Plyusnin, P. E.; Ogienko, A. G. The Thermodynamic Stability of Inclusion Compounds of Zinc(II) and Nickel(II) Coordination Polymers with Chlorobenzene as a Guest: The Determination of Guest Vapor Pressure by the Tensimetric Method. *Russ. J. Phys. Chem. A* **2006**, *80*, 1920–1924.

(12) Mochida, T.; Qiu, Y.; Funasako, Y.; Inokuchi, M.; Noguchi, M.; Fujimori, H.; Furushima, Y. Ionic Liquid-Containing Coordination Polymer: Solvent-Free Synthesis, Incongruent Melting, and Glass Formation. *Chem. Commun.* **2022**, *58*, 6725–6728.

(13) Marszalek, M.; Fei, Z.; Zhu, D.-R.; Scopelliti, R.; Dyson, P. J.; Zakeeruddin, S. M.; Grätzel, M. Application of Ionic Liquids Containing Tricyanomethanide $[C(CN)_3]^-$ or Tetracyanoborate

$[B(CN)_4]^-$ Anions in Dye-Sensitized Solar Cells. *Inorg. Chem.* **2011**, *50*, 11561–11567.

(14) *Fast Scanning Calorimatry*, 1st ed.; Schick, C. S., Mathot, V., Eds.; Springer, 2016.

(15) Nozari, V.; Calahoo, C.; Tuffnell, J. M.; Keen, D. A.; Bennett, T. D.; Wondraczek, L. Ionic Liquid Facilitated Melting of the Metal-Organic Framework ZIF-8. *Nat. Commun.* **2021**, *12*, 5703.

(16) Mori, S.; Obora, T.; Namaki, M.; Kondo, M.; Moriya, M. Organic Crystalline Solid Electrolytes with High Mg-Ion Conductivity Composed of Nonflammable Ionic Liquid Analogs and $Mg(TFSA)_2$. *Inorg. Chem.* **2022**, *61*, 7358–7364.

(17) Batten, S. R.; Murray, K. S. Structure and Magnetism of Coordination Polymers Containing Dicyanamide and Tricyanomethanide. *Coord. Chem. Rev.* **2003**, *246*, 103–130.

(18) (a) de Tacconi, N. R.; Rajeshwar, K.; Lezna, R. O. Metal Hexacyanoferrates: Electrosynthesis, in Situ Characterization, and Applications. *Chem. Mater.* **2003**, *15*, 3046–3062. (b) Iwamoto, T. Past, Present and Future of the Clathrate Inclusion Compounds Built of Cyanometallate Hosts. *J. Inclusion Phenom. Mol. Recognit. Chem.* **1996**, *24*, 61–132. (c) Yoshikawa, H.; Nishikiori, S.-I.; Suwinska, K.; Luboradzki, R.; Lipkowski, J. Crystal Structure of a Polycyano–Polycadmate Hostclathrate Including a Charge-Transfer Complex of Methylviologen Dicationand Mesitylene as a Guest. *Chem. Commun.* **2001**, 1398–1399.

(19) Shaw, B. K.; Hughes, A. R.; Ducamp, M.; Moss, S.; Debnath, A.; Sapnik, A. F.; Thorne, M. F.; McHugh, L. N.; Pugliese, A.; Keeble, D. S.; Chater, P.; Bermudez-Garcia, J. M.; Moya, X.; Saha, S. K.; Keen, D. A.; Coudert, F.-X.; Blanc, F.; Bennett, T. D. Melting of Hybrid Organic-Inorganic Perovskites. *Nat. Chem.* **2021**, *13*, 778–785.

(20) Wineinger, H. B.; Smetana, V.; Nayak, A.; Qu, F.; Mudring, A.-V.; Rogers, R. D. Accessing Lanthanide Tricyanomethanide Coordination Polymers Using Ionic Liquids. *Cryst. Growth Des.*

2022, *22*, 2372–2381.

(21) (a) Shan, N.; Toda, F.; Jones, W. Mechanochemistry and Co-Crystal Formation: Effect of Solvent on Reaction Kinetics. *Chem. Commun.* **2002**, 2372–2373. (b) Braga, D.; Maini, L.; Grepioni, F. Mechanochemical Preparation of Co-Crystals. *Chem. Soc. Rev.* **2013**, *42*, 7638–7648.

(22) Blatov, V. A.; Shevchenko, A. P.; Proserpio, D. M. Applied Topological Analysis of Crystal Structures with the Program Package ToposPro. *Cryst. Growth Des.* **2014**, *14*, 3576–3586.

(23) Witt, J. R.; Britton, D. The Crystal Structure of Potassium Tricyanomethide, $KC(CN)_3$. *Acta Crystallogr. B* **1971**, *27*, 1835–1836.

(24) Yoshida, Y.; Muroi, K.; Otsuka, A.; Saito, G.; Takahashi, M.; Yoko, T. 1-Ethyl-3-Methylimidazolium Based Ionic Liquids Containing Cyano Groups: Synthesis, Characterization, and Crystal Structure. *Inorg. Chem.* **2004**, *43*, 1458–1462.

(25) Zhao, Y.; Gani, R.; Afzal, R. M.; Zhang, X.; Zhang, S. Ionic Liquids for Absorption and Separation of Gases: An Extensive Database and a Systematic Screening Method. *AIChE J.* **2017**, *63*, 1353–1367.

(26) Turnbull, D.; Cohen, M. H. Crystallization Kinetics and Glass Formation. In *Modern Aspects of the Vitreous State*, 1 st ed.; Butterworth, **1960**, pp. 73–74.

(27) Sheldrick, G. M. A Short History of SHELX. *Acta Crystallogr.*, **2008**, A*64*, 112–122.

(28) Macrae, C. F.; Bruno, I. J.; Chisholm, J. A.; Edgington, P. R.; McCabe, P.; Pidcock, E.; Rodriguez-Monge, L.; Taylor, R.; Streek, J. van de; Wood, P. A. Mercury CSD 2.0 – New Features for the Visualization and Investigation of Crystal Structures. *J. Appl. Crystallogr.* **2008**, *41*, 466–470.

(29) Spek, A. L. Structure Validation in Chemical Crystallography. *Acta Crystallogr.* **2009**,

D*65*, 148–155.

TOC

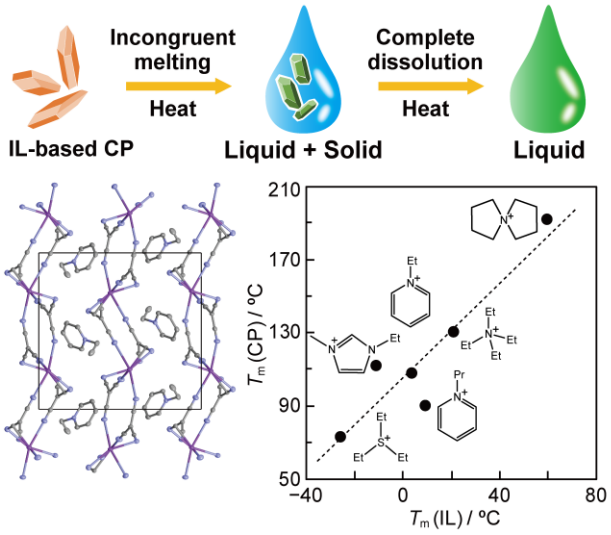

We synthesized ionic-liquid-containing melting coordination polymers and elucidated the factors governing their melting points, the mechanism of decomposition melting, and the conditions of vitrification.

Supporting Information

Incongruent Melting and Vitrification Behaviors of Anionic Coordination Polymers Incorporating Ionic Liquid Cations

Tomoyuki Mochida,*[†‡] Yi Qiu,[†] Ryo Sumitani,[†] Hironori Kimata,[†] and Yoshitomo Furushima[#]

[†]*Department of Chemistry, Graduate School of Science, Kobe University, 1-1 Rokkodai, Nada, Kobe, Hyogo 657-8501, Japan. E-mail: tmochida@platinum.kobe-u.ac.jp*

[‡]*Research Center for Membrane and Film Technology, Kobe University, 1-1 Rokkodai, Nada, Kobe, Hyogo 657-8501, Japan*

[#]*Materials Characterization Laboratories, Toray Research Center Inc., 3-7, Sonoyama 3-chome, Otsu, Shiga 520-8567, Japan*

Contents

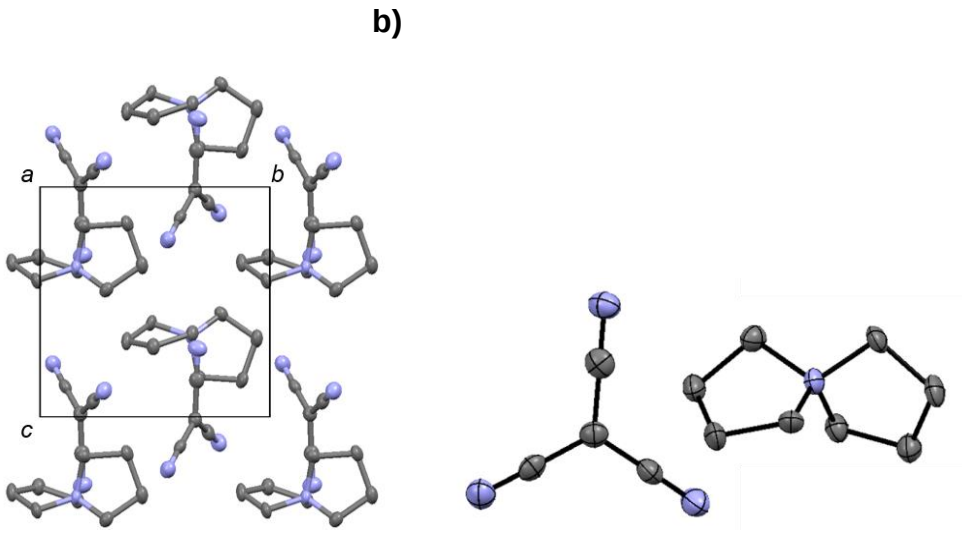

Fig. S1. Crystal structure of $[N(C_4H_8)_2][TCM]$ determined at −183 °C. (a) The packing diagram, and (b) the ORTEP drawing of the molecular structure.

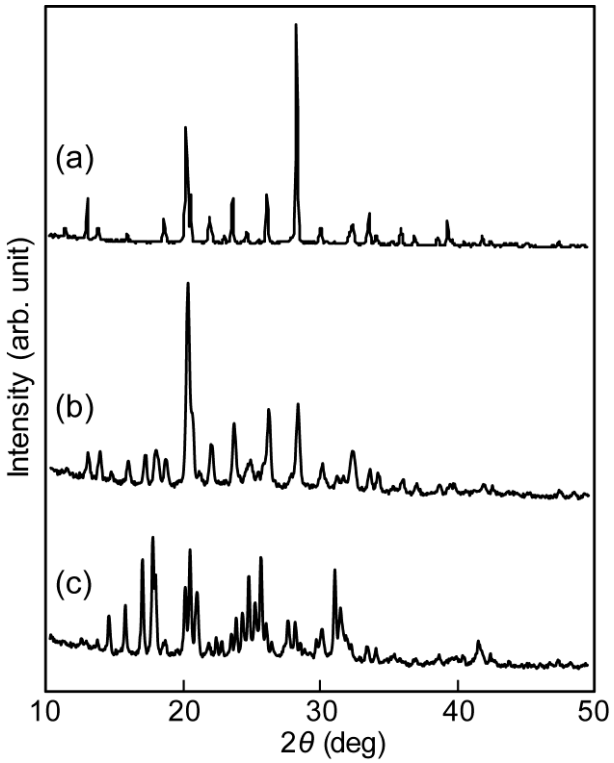

Fig. S2. PXRD patterns of (a) **1-N(C$_4$H$_8$)$_2$** simulated from its crystal structure at −173 °C, (b) the mixture of $[N(C_4H_8)_2][TCM]$ and K[TCM] ground under an air atmosphere for 0.5 h, and (c) the mixture ground under an argon atmosphere for 0.5 h.

a) 1-EtPy

30 °C 112 °C 231 °C 70 °C 107 °C

b) 1-NEt_4

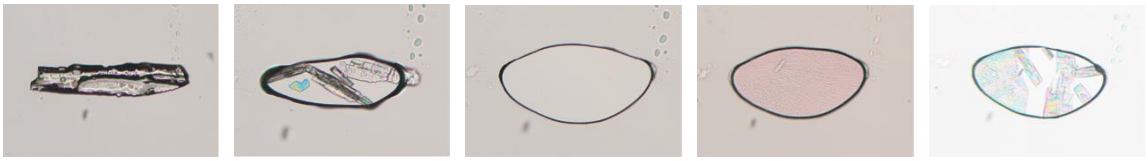

20 °C 136 °C 241 °C 122 °C 132 °C

Fig. S3. POM images of (a) **1-EtPy** and (b) **1-NEt_4**. From left to right: crystalline state, incongruent melting, complete melting, solidification (taken upon cooling of the liquid), and incongruent melting (taken upon reheating of the solid).

a) b) c) d) e)

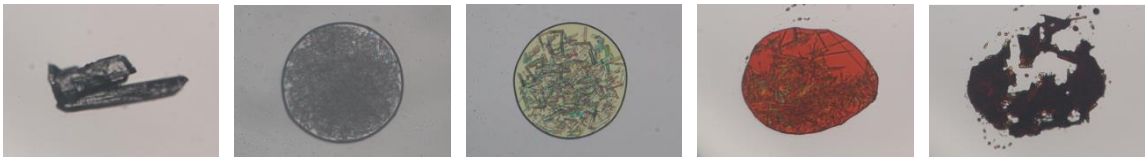

20 °C 88 °C 181 °C 195 °C 233 °C

Fig. S4. POM images of **1-SEt_3**. (a) Crystalline state, (b) incongruent melting, and (c–e) gradual pyrolysis.

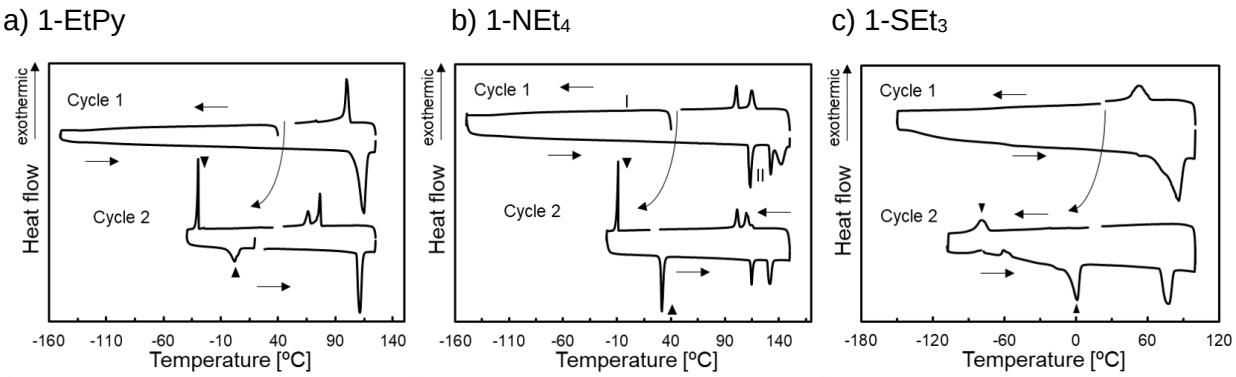

Fig. S5. DSC traces of (a) **1-EtPy**, (b) **1-NEt4**, and (c) **1-SEt3**. Solid triangles indicate the solidification and melting of the IL component.

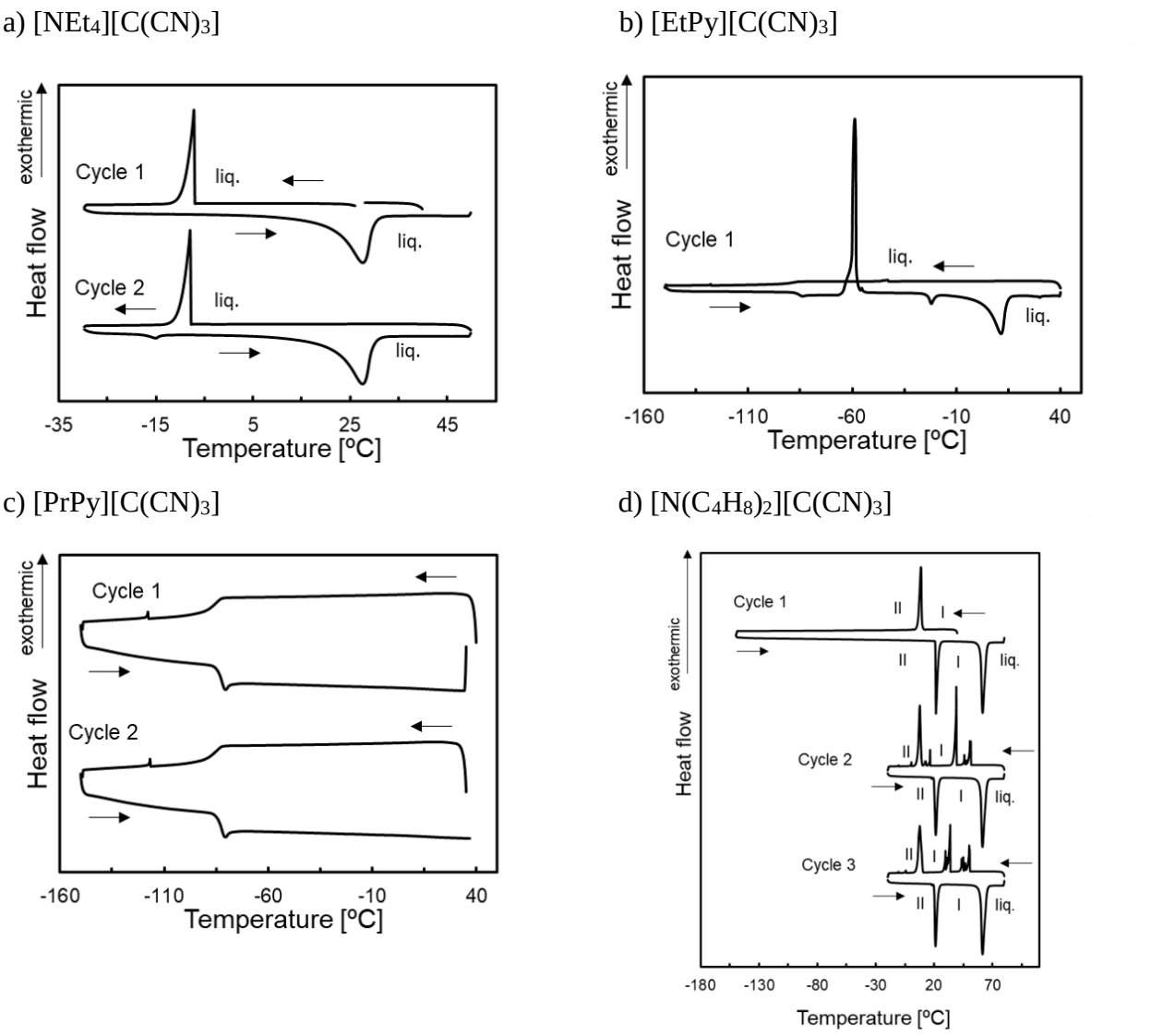

Fig. S6. DSC traces of (a) [NEt4][C(CN)3], (b) [EtPy][C(CN)3], (c) [PrPy][C(CN)3], and (d) [N(C4H8)2][C(CN)3].

Table S1. Crystallographic parameters

	1-NEt$_4$	**1-EtPy**	**1-PrPy**
Empirical formula	$C_{16}H_{20}N_7K$	$C_{15}H_{10}N_7K$	$C_{16}H_{12}N_7K$
Formula weight	349.49	327.40	341.43
Crystal system	Orthorhombic	Monoclinic	Monoclinic
Space group	*P*na2$_1$	*P*2$_1$/*n*	*P*2$_1$/*n*
a (Å)	16.2658(13)	7.9947(13)	8.058(4)
b (Å)	8.8972(7)	14.298(2)	14.234(7)
c (Å)	13.1945(11)	14.912(2)	15.216(7)
α (°)	90	90	90
β (°)	90	93.496(2)	92.156(7)
γ (°)	90	90	90
V (Å^3)	1909.5(3)	1701.4(5)	1744.0(15)
Z	4	4	4
ρ_{calcd} (g cm^{-3})	1.216	1.278	1.300
F (000)	736	672	704
Reflections collected	10113	9134	6958
Independent reflections	3918	3587	3474
Parameters	221	209	218
Temperature (K)	100	100	100
R_1[a], R_w[b] ($I > 2\sigma$)	0.0193, 0.0505	0.0262, 0.0714	0.0470, 0.1115
R_1[a], R_w[b] (all data)	0.0199, 0.0509	0.0269, 0.0721	0.0593, 0.1218
Goodness of fit	1.033	1.049	1.085
$\Delta\rho_{max,min}$ [e Å^{-3}]	0.113, −0.137	0.195, −0.300	0.646, −0.505

[a] $R_1 = \Sigma||F_o| - |F_c|| / \Sigma|F_o|$; [b] $R_w = [\Sigma w (F_o^2 - F_c^2)^2 / \Sigma w (F_o^2)^2]^{1/2}$.

Table S2. Crystallographic parameters

	1-SEt$_3$	**1-N(C$_4$H$_8$)$_2$**	**[N(C$_4$H$_8$)$_2$][C(CN)$_3$]**
Empirical formula	$C_{15}H_{17}N_6KS$	$C_{16}H_{16}N_7K$	$C_{12}H_{16}N_4$
Formula weight	352.5	345.46	216.29
Crystal system	Orthorhombic	Triclinic	Monoclinic
Space group	*P*nma	*P*-1	$P2_1$
a (Å)	16.506(2)	7.976(2)	9.050(8)
b (Å)	8.7998(12)	8.477(3)	8.155(7)
c (Å)	12.1213(17)	13.015(4)	9.145(8)
α (°)	90	96.612(6)	90
β (°)	90	90.222(4)	117.961(10)
γ (°)	90	97.026(5)	90
V (Å^3)	1760.6(4)	867.4(4)	596.1(9)
Z	4	2	2
ρ_{calcd} (g cm^{-3})	1.33	1.323	1.205
F (000)	736	360	232
Reflections collected	19562	3200	1597
Independent reflections	2224	2929	1560
Parameters	140	218	148
Temperature (K)	90	100	90
R_1[a], R_w[b] ($I > 2\sigma$)	0.0712, 0.2030	0.0274, 0.0773	0.0587, 0.1474
R_1[a], R_w[b] (all data)	0.0730, 0.2049	0.0304, 0.0796	0.0765, 0.1602
Goodness-of-fit	1.131	1.068	1.084
$\Delta\rho_{max,min}$ [e Å^{-3}]	1.242, −1.671	0.228, −0.223	0.210, −0.209

[a] $R_1 = \Sigma||F_o| - |F_c|| / \Sigma|F_o|$; [b] $R_w = [\Sigma w (F_o^2 - F_c^2)^2 / \Sigma w (F_o^2)^2]^{1/2}$.